


## Article

# Effects of Build Direction and Heat Treatment on the Defect Characterization and Fatigue Properties of Laser Powder Bed Fusion Ti6Al4V

Wenbo Sun <sup>1</sup> , Yu'e Ma <sup>2,\*</sup>, Peiyao Li <sup>2</sup>, Ziad Moumni <sup>1,3</sup> and Weihong Zhang <sup>1,\*</sup><sup>1</sup> State IJR Center of Aerospace Design and Additive Manufacturing, School of Mechanical Engineering, Northwestern Polytechnical University, Xi'an 710072, China; wenbo-sun@nwpu.edu.cn (W.S.)<sup>2</sup> School of Aeronautics, Northwestern Polytechnical University, Xi'an 710072, China<sup>3</sup> Mechanical Engineering Department, ENSTA-Paris Institut Polytechnique de Paris, 91120 Palaiseau, France

\* Correspondence: ma.yu.e@nwpu.edu.cn (Y.M.); zhangwh@nwpu.edu.cn (W.Z.)

**Abstract:** Laser powder bed fusion (LPBF) is one of the high-precision additive manufacturing techniques for producing complex 3D components. It is well known that defects appear in additive-manufactured parts, and they deeply affect the fatigue properties; even heat treatment is performed after printing. In order to meet the safe-life design requirements of additive-manufactured aircraft structures, the effects of build direction and heat treatment on defects and fatigue properties need to be quantified. Hence, Ti6Al4V alloy samples with different build directions were designed and printed by LPBF. X-ray computed tomography was used to quantitatively analyze the defect size, the sphericity, and the defect orientation. And their effects on fatigue properties were studied. An extended effective defect size and a defect-based fatigue anisotropy evaluation process are proposed to qualify the effects of the defect size, sphericity, and defect orientation. It is shown that the build direction can affect the porosity distribution and maximum defect size, while the annealing treatment can cause the coalescence of small defects and higher porosity. The defect orientation exhibited a fluctuating trend of  $0^{\circ}$ – $90^{\circ}$ – $0^{\circ}$ – $90^{\circ}$ – $0^{\circ}$  as the volume increased. The elongated lack of fusion defects related to the build direction was the main crack source and could lead to fatigue anisotropy of LPBF Ti6Al4V.

**Keywords:** defect distribution; build direction; laser powder bed fusion Ti6Al4V; fatigue; anisotropy



**Citation:** Sun, W.; Ma, Y.; Li, P.; Moumni, Z.; Zhang, W. Effects of Build Direction and Heat Treatment on the Defect Characterization and Fatigue Properties of Laser Powder Bed Fusion Ti6Al4V. *Aerospace* **2024**, *11*, 854. <https://doi.org/10.3390/aerospace11100854>

Academic Editors: Fernando Mas and Khamis Essa

Received: 3 September 2024

Revised: 6 October 2024

Accepted: 8 October 2024

Published: 16 October 2024



**Copyright:** © 2024 by the authors. Licensee MDPI, Basel, Switzerland. This article is an open access article distributed under the terms and conditions of the Creative Commons Attribution (CC BY) license (<https://creativecommons.org/licenses/by/4.0/>).

## 1. Introduction

The additive-manufactured (AM) Ti6Al4V titanium alloy has been widely used in the aerospace and biomedical industries due to its excellent corrosion resistance and high specific strength. Compared with conventionally manufactured parts, a finer microstructure of AM metal materials can be produced by using the optimized processing parameters, and a promising static mechanical performance can be obtained. However, the defects in AM metal alloys can lead to the degradation of fatigue properties and an anisotropic mechanical response [1–5].

During laser powder bed fusion, the powders are deposited on top of the substrate materials and then melted by the laser beam. The insufficient overlap and inadequate energy input cause lack of fusion (LoF) defects with large, irregular, and sharp shapes. However, over-melting causes gas-entrapped pores with a near-spherical morphology [6–8]. Chen [9] used in situ monitoring, ex situ surface topography, and  $\mu$ -CT to investigate the mechanisms of LoF defect formation and evolution, and found that LoF defects are formed due to the discontinuities between the adjacent deposition layers. At present, LoF and pore defects are inevitable in AM metals because of the unstable input energy densities and the complexity of the multi-physics fields [10]. LoF defects are prone to appearing at the laser track between the adjacent laser paths and the consecutive depositions because

the liquid metal shrinks during cooling [11], and the majority of LoF defects are formed perpendicularly to the build direction [12,13]. The coalescence and agglomeration of the defects can be observed in the subsurface region and the support-connected areas, where the unstable laser energy increases porosity [3,14]. It was revealed by Malashin [15] that a higher thermal impact on the powder increases the likelihood of defects.

The maneuverability of additive manufacturing makes it possible to control porosity by optimizing the processing parameters [16] and the contouring passes [17]. Several researchers have studied the effect of laser parameters on porosity [3,6,10,11,16], and they have found that the energy density  $E_v$  can be used to optimize the total porosity of AM alloys as a function of the laser power  $P$ , the scanning speed  $v$ , the hatch distance  $h$ , and the layer thickness  $t$ :

$$E_v = \frac{P}{v \cdot h \cdot t} \quad (1)$$

The defect size decreases with a steep slope as the energy density increases to a certain value and then starts to increase with a lower slope with a further increase in the energy density [6,10]. The porosity can be effectively reduced by the optimized processing parameters, the new subsequent layer, and the thermal cycle [18,19]. It shows that laser power and velocity are two dominant factors [14,20,21]. Du [16] found that laser power has the largest effect on porosity, while Kasperovich [10] found that velocity exerts the most dominant influence on the porosity fraction. In addition, the melt pool characterization, such as the melt pool area [7] and the solidification [22], also has a non-negligible effect on the defect.

Post-treatment, as an important technique to improve the mechanical performance of metal alloys, also has a significant effect on the porosity of AM alloys. There are two common heat treatments: one is hot isostatic pressing (HIP) and the other one is annealing heat treatment. Consistent conclusions [3,6,17,23–25] have been drawn: the HIP process can drastically reduce or heal defects, especially the trapped gas porosity, but it has little effect on the subsurface defects [3] and LoF defects [17]. However, the effect of the annealing heat treatment on defects has seldom been discussed in the literature.

The X-ray computed tomography (CT) technique is an efficient method to obtain the defect information of AM metal alloys [26]. Despite the disorganized spatial distribution of defects [18,27–29], it is possible to quantify the distribution of their features, such as the defect shape [14], the defect orientation [30,31], and the defect position [27,32]. It was found that the population of defects was dominated by the trapped gas pores, while the crack and damage initiation of AM alloys resulted from LoF defects. The size and shape of defects can be mathematically characterized by the equivalent diameter [33], the sphericity [23], the aspect ratio [18], and so on. Seifi [33] correlated defect size with build height and found that the transient thermal evolution made the largest defect size located in the middle section of the sample considered [34]. The statistical distribution of pores can be fitted by the normal distribution [35], the exponential distribution [36], and the logarithmic normal distribution [27,30,32] according to the difference in sample size and the accuracy of the measuring equipment. Xu [37] characterized the defect  $\sqrt{aera}$  by the Weibull distribution and found that the 45° sample had a higher defect size than the 0° sample and the 90° sample. Both the sphericity and the aspect ratio of AM metal defects typically decreased with an increase in the defect size [18].

Due to the high stress concentration at defect tips, the detrimental effect of defects on mechanical properties [38], especially fatigue performance [39–42], has been widely studied. Not only defect size can cause the scattering of the fatigue life [43–45], but also spatial distribution [46–48]. The strain localization around a defect leads to premature fatigue failure, and LoF defects exhibited 27.8% higher values than other pores of the same size [49]. However, when the defect size is below a critical threshold, it will not cause fatigue failure [50]. A comprehensive understanding of the defect distribution of AM alloys can improve the prediction accuracy of fatigue life. Zou [51] found that the defect location was the main factor that affected the fatigue performance and established the

relationship between critical defect characteristics and the fatigue life of the LPBF alloy. Afazov [52] introduced a defect factor and successfully predicted the fatigue performance based on defect size and location from the surface. Nadot [53] proposed a defect-based fatigue criterion through the local stress gradient, and placed emphasis on the effect of micro-defects on the fatigue limit of metallic materials. Based on the Murakami model, Teschke [54] and Sanaei [55] investigated the sensitivity of assumed defect size and shape to fatigue predictions, and found that fatigue life of AM alloys can be more accurately evaluated through the square root of area obtained from extreme value statistics. Moreover, Wu [56] presented further evidence to substantiate the effect of microstructural defects on fatigue strength of LPBF Ti6Al4V alloys by time-lapse synchrotron radiation X-ray microtomography.

Despite lots of studies having been conducted on the defect-based fatigue analysis of LPBF Ti6Al4V, the effects of build direction and annealing heat treatment on defect distribution are still insufficient. In addition, the contribution of defect characteristics to the fatigue anisotropy of LPBF Ti6Al4V was seldom discussed, and the orientation and aspect ratio of defects should be considered in the defect-based life prediction model. To overcome this challenge, an extended Murakami model and a defect-based fatigue anisotropy evaluation approach were proposed in this study. LPBF Ti6Al4V titanium alloys in 0°, 45°, and 90° build directions were designed and manufactured, and annealing heat treatment was conducted. The defect distributions of as-built samples and heat-treated samples along the build direction and radial direction were compared based on X-ray computed tomography. The defect size, sphericity, and defect orientation were measured and quantified. Finally, an extended square root of defect area, an alternative to the Murakami size, was characterized by a combination of the defect location, defect orientation, and defect aspect ratio. The anisotropy of fatigue limit was successfully predicted based on the defect distribution.

2. Materials and Methods

2.1. Sample Design

Commercial BLT-TC4 powder (Bright Laser Technologies Co., Ltd., Xi'an, China) was used in this study. The powder size distribution range was 20–53 μm, and the chemical compositions of Ti6Al4V powder are listed in Table 1. All samples were manufactured by the same parameters and on the same substrate to ensure that build direction was the only influencing factor during LPBF. A BLT-S310 machine (Bright Laser Technologies Co., Ltd., Xi'an, China) and optimized processing parameters were used in this study, as shown in Figure 1a. All samples were printed with the same laser parameters in nitrogen gas conditions, and 80 °C preheating of the substrate was conducted. During printing, the oxygen level was less than 100 ppm. The laser power was 350 W, the laser beam diameter was 80 μm, and the scanning speed was kept at 1000 mm/s. A cross-hatch pattern scanning strategy was used with a 60 μm thick layer, as shown in Figure 1b.

Table 1. Chemical compositions of Ti6Al4V powders (wt %).

(%)							
Ti balance	Al 5.5–6.75	V 3.5–4.5	Fe ≤0.30	C ≤0.08	H ≤0.015	O ≤0.20	N ≤0.05

LPBF Ti6Al4V cylindrical specimens in 0°, 45°, and 90° build directions were fabricated. To maintain the structural integrity and printability of the 0° sample and the 45° sample, additional support structures were built, as shown in Figure 1c. After all samples were printed, the as-built samples were cooled in argon gas conditions to room temperature without any other treatment. The heat-treated samples were held at 800 ± 5 °C for 4 h and then cooled in argon gas conditions to room temperature.

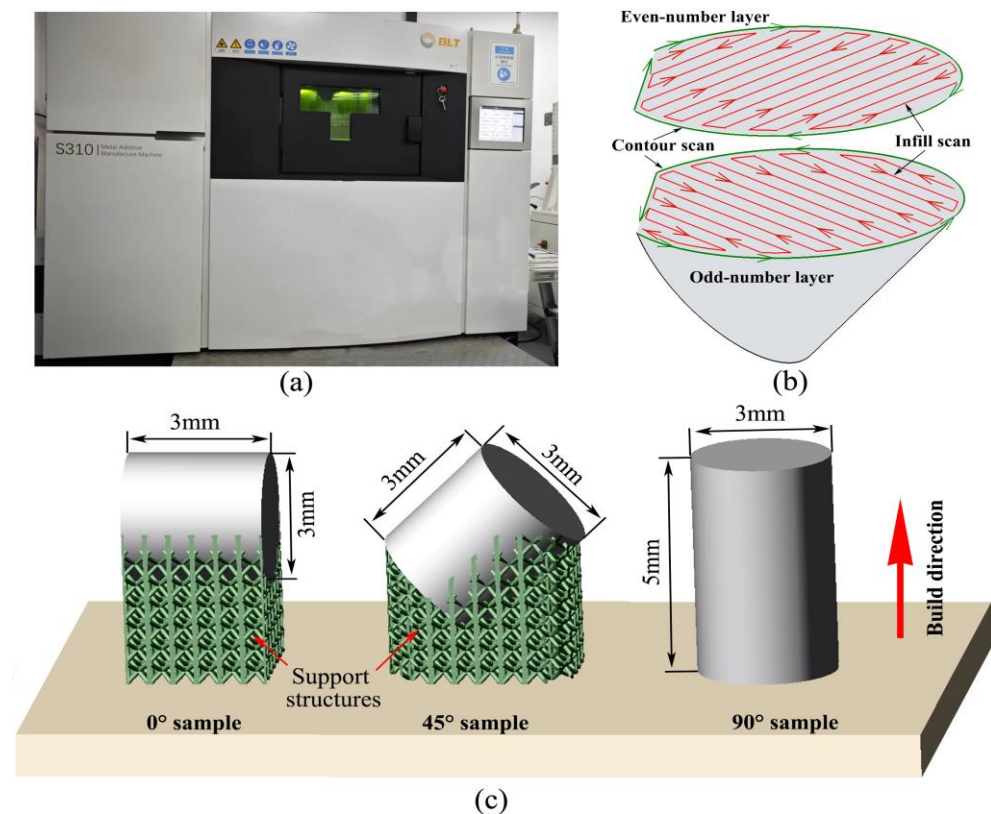


**Figure 1.** Set-up, (a) BLT-S310 machine, (b) the scanning strategies, (c) the sample design.

## 2.2. Defect Detection and Analysis

An X-ray CT modeled as ZEISS Xradia 520 Versa (Carl Zeiss Microscopy GmbH, Jena, Germany) was used to detect the porosity and defects of the LPBF Ti6Al4V titanium alloy in different build directions and heat treatment conditions. The reconstructed 3D samples are shown in Figure 2. A resolution of  $5.89 \mu\text{m}$  per voxel was adopted to capture small-scale defects with  $10 \mu\text{m}$  or larger diameter. Dragonfly software (Version 2021.1) [57] was used to reconstruct the spatial distribution of AM defects. The defect volume, surface area, and defect coordinate were statistically analyzed and compared. The Feret diameter, derived from the distance of two tangents to the contour of a defect in a well-defined orientation, was measured to characterize the defect size. All statistical data were analyzed by Origin software (Learning edition, Version 2021 beta 1), and an R-square larger than 0.95 was considered statistically significant.

## 2.3. Defect-Based Fatigue Limit Analysis

Murakami [58] proposed the square root of defect area,  $\sqrt{\text{area}}$ , as the defect size, and it is an important parameter used in fatigue life prediction models of metal materials with defects.

Extreme value statistics were performed first to obtain the effective defect size. The largest extreme value distribution of defects can be expressed using the Gumbel function:

$$G(x) = \exp(-\exp(-(x - \mu)/\beta)) \quad (2)$$

where  $\mu$  and  $\beta$  are the location and scale parameters, respectively.



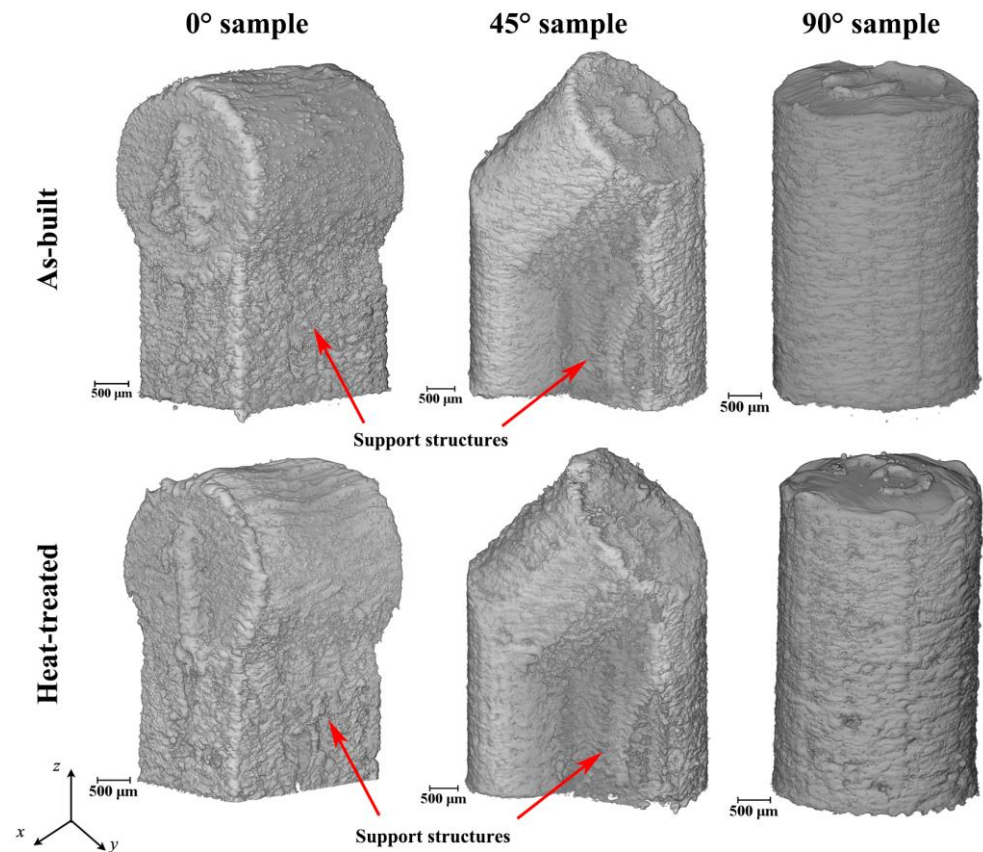


**Figure 2.** The reconstructed 3D samples in different build directions and heat treatment conditions.

The tested sample will be divided into several regions according to the sample size. In each region, the projection area of each defect is obtained, and the extreme value of  $\sqrt{area_{eff}}$  is calculated. The maximum defects in all regions are arranged in ascending order:  $\sqrt{area_{eff-i}}, i = 1, 2, 3, \dots, n$ . The cumulative distribution function  $G(x)$  can be expressed as follows:

$$G(\sqrt{area_i}) = i/(n+1) = \exp(-\exp(-(\sqrt{area_i} - \mu)/\beta)) \quad (3)$$

And then, the reduced variate  $y$  is obtained:

$$y = -\ln(-\ln G(\sqrt{area_i})) = (\sqrt{area_i} - \mu)/\beta \quad (4)$$

According to the Murakami model [58], the stress intensity factor (SIF) can be calculated by using  $\sqrt{area_{eff}}$ :

$$\Delta K_{eff} = C_1 \Delta \sigma \sqrt{\pi \sqrt{area_{eff}}} \quad (5)$$

where  $C_1$  is a constant related to defect position, equal to 0.5 for internal defect and 0.65 for surface defect.

The threshold of SIF for a short crack can be expressed as follows:

$$\Delta K_{th} = C_2 (HV + 120) (\sqrt{area})^{1/3} \quad (6)$$

Combining Equations (5) and (6), the fatigue limit  $\sigma_w$  can be expressed as follows:

$$\sigma_w = \frac{C \cdot (HV + 120)}{(\sqrt{area})^{1/6}} \quad (7)$$

where  $C$  is a constant related to defect position, equal to 1.41, 143, and 1.56 for the surface defect, subsurface defect, and internal defect separately.  $HV$  is Vickers hardness, and the microhardness of AM Ti6Al4V is about 370  $HV$  [59].

### 3. Results and Discussion

#### 3.1. Defect Reconstruction

The defects in all kinds of samples were segmented by interactive thresholding with the intensity range from 12,000 to 35,000 after the spatial reconstructions were conducted. The surface roughness effect on defect was not considered in this study, and a 100  $\mu\text{m}$  thick “ring” region from the sample surface was cut to remove the rough surface as printed. In addition, the median filter was applied to avoid artifacts. Small defects with a diameter below 10  $\mu\text{m}$  were not counted.

The defects of all samples were extracted, and the spatial distribution with respect to their volume is shown in Figure 3. The as-built samples are shown in Figure 3a–c, and the heat-treated samples are shown in Figure 3d–f. The maximum volumes of the 0° as-built sample and the 45° as-built sample are about  $8.5 \times 10^5 \mu\text{m}^3$  and  $8.2 \times 10^5 \mu\text{m}^3$ , respectively, while that of the 90° sample is  $5.3 \times 10^5 \mu\text{m}^3$ , much lower than that of the 0° and 45° samples. After the samples were heat-treated, the maximum volume of defect in the 0° sample and the 45° sample increased to  $2.4\text{--}2.9 \times 10^6 \mu\text{m}^3$ , as shown in Figure 3d,e. The defect size in the 90° sample increased to  $4.8 \times 10^6 \mu\text{m}^3$ , almost nine times that of the as-built one, shown in Figure 3f. The heat treatment can enlarge the defect size of the LPBF Ti6Al4V titanium alloy.

The geometrical dimensions and defect statistics are listed in Table 2. It is shown that both the counts and total volume of defects in the 45° sample are the lowest. After heat treatment, the defect number was reduced, while larger defects were presented both in these three build direction samples. These large defects have irregular shapes, but are prone to growing along the build direction, as shown in Figure 3d,f.

**Table 2.** Geometry and defect data of the tested samples.

Types	Build Direction	Geometry of Tested Sample		Defects		Porosity (%)
		Diameter ( $10^3 \mu\text{m}$ )	Height ( $10^3 \mu\text{m}$ )	Total Volume ( $10^7 \mu\text{m}^3$ )	Counts	
As-built	0°	3.0	2.9	3.6	930	0.180
	45°	2.9	3.0	2.9	649	0.152
	90°	2.9	4.3	3.1	1426	0.108
Heat-treated	0°	2.8	2.9	3.8	362	0.210
	45°	2.9	2.8	2.9	335	0.155
	90°	3.0	4.6	11.4	1160	0.360

#### 3.2. Spatial Distribution

##### 3.2.1. Porosity

In Figure 4, the relationship between porosity and build direction is shown. The porosity of as-built samples ranged from 0.108% to 0.180%. When heat treatment is performed, high temperature can cause the coalescence of initial cracks into a bigger one and lead to higher porosity. The porosity of heat-treated samples ranged from 0.155% to 0.360%. It is particularly noted that the porosity of the 90° sample increased more than three times after annealing treatment, due to a large number of defects in the 90° sample.

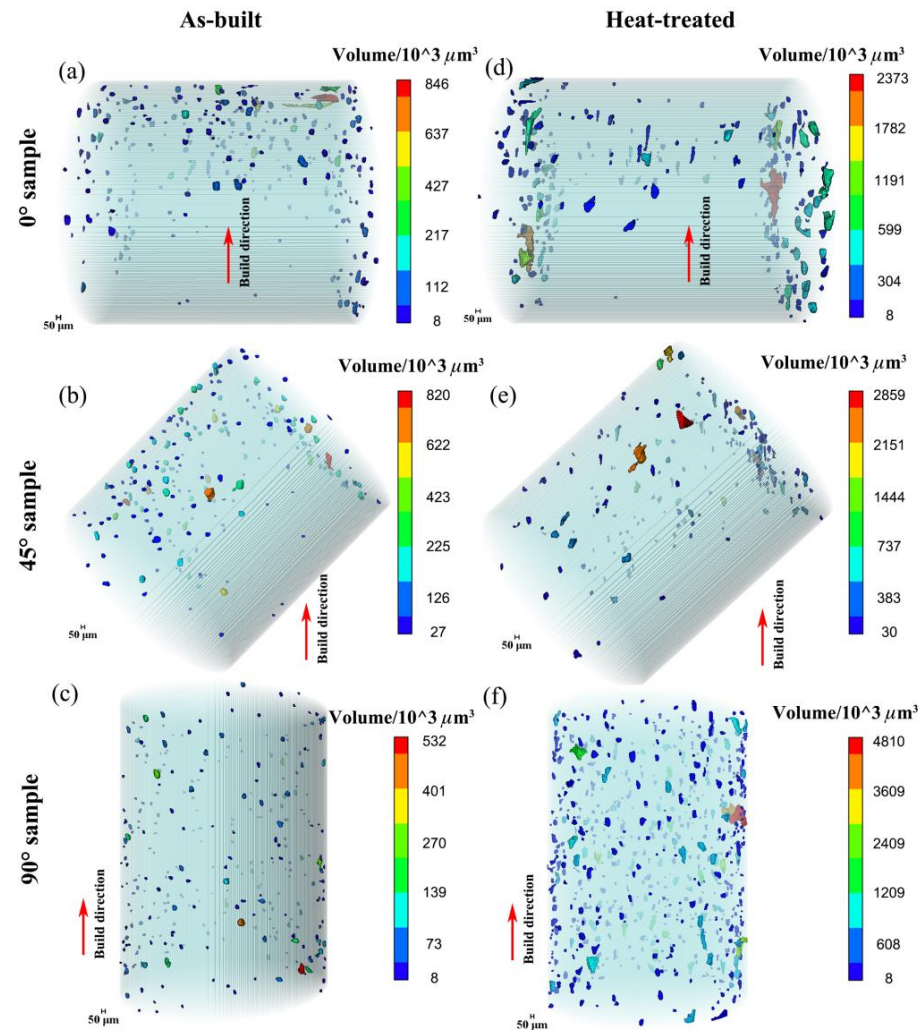


**Figure 3.** Defect distribution of LPBF Ti6Al4V in different build directions and heat treatment conditions: (a) 0° as-built, (b) 45° as-built, (c) 90° as-built, (d) 0° heat-treated, (e) 45° heat-treated, (f) 90° heat-treated.

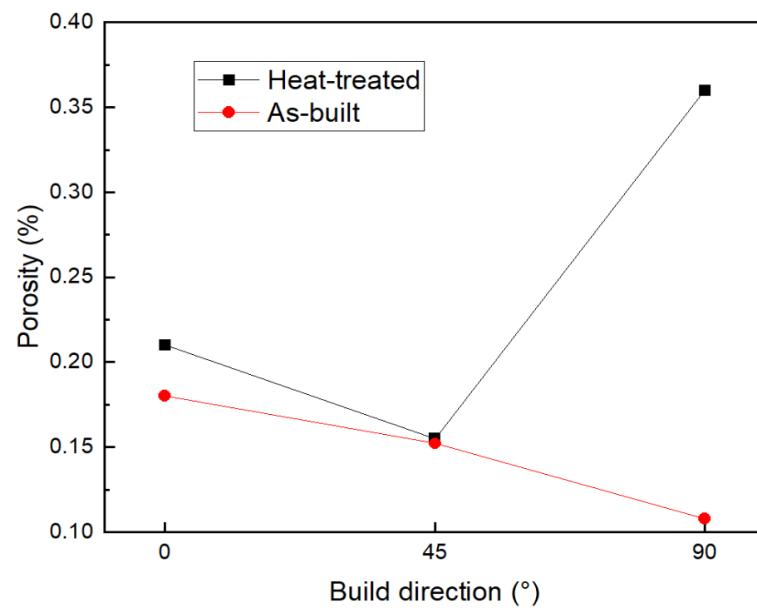


**Figure 4.** Effect of build direction and heat treatment on porosity.

### 3.2.2. Defect Distribution along the Build Direction

The orthographic projection of defects was performed on the vertical plane, and the porosity distribution along the build direction was plotted, as shown in Figure 5. For the 0° sample in Figure 5a,d, there are more defects in the upper region and ends of samples. The maximum Feret diameter of the 0° sample was about 500  $\mu\text{m}$  in both conditions. The porosity curves of the 0° as-built sample and the 0° heat-treated sample showed a similar tendency, and the porosity value ranged from 0 to 0.5%, as shown in Figure 5g. The curve fluctuated periodically along the build direction, and the distance between adjacent peaks was a multiple of the 60  $\mu\text{m}$  thick layer, as shown in Figure 5g.

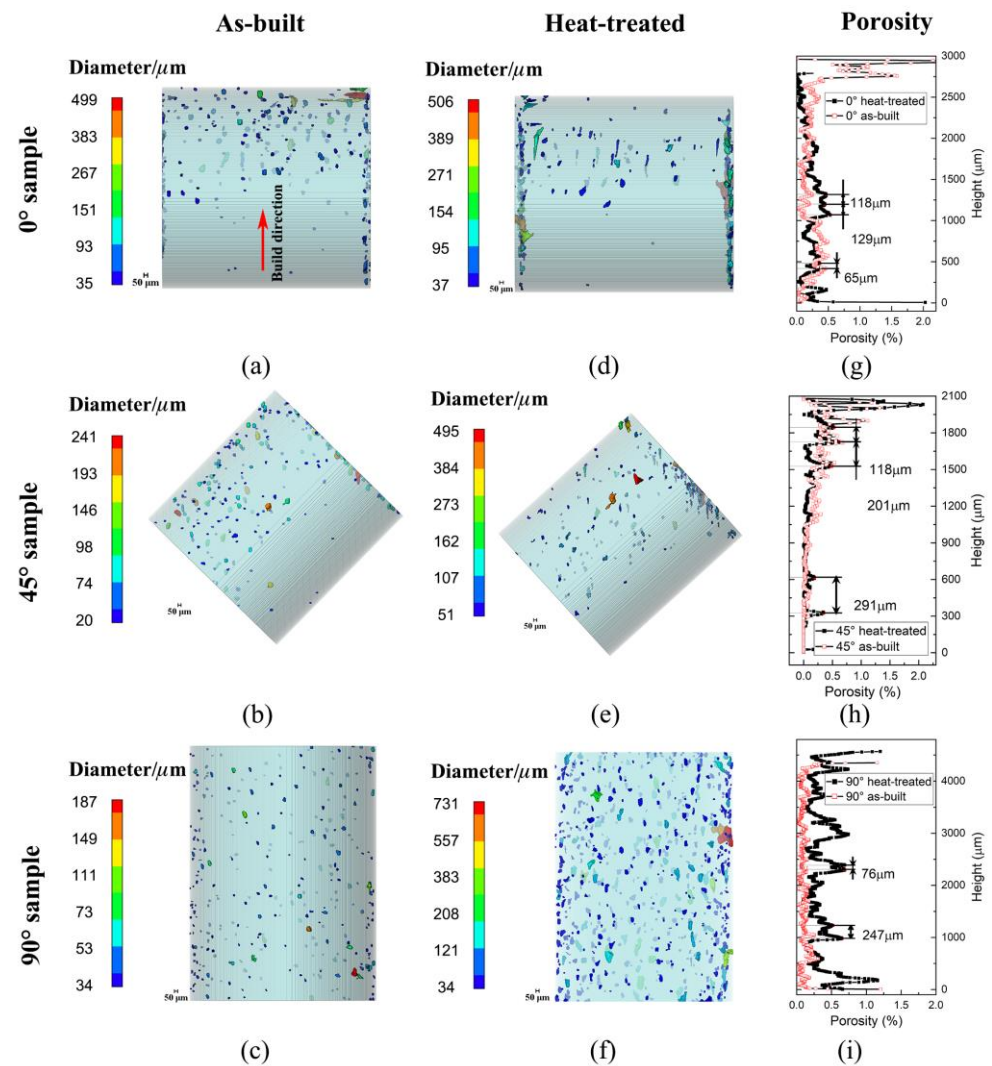


**Figure 5.** Orthographic projection of defects along the build direction: (a) the 0° as-built sample, (b) the 45° as-built sample, (c) the 90° as-built sample, (d) the 0° heat-treated sample, (e) the 45° heat-treated sample, (f) the 90° heat-treated sample, (g) porosity curves in the 0° samples, (h) porosity curves in the 45° samples, (i) porosity curves in the 90° samples.

For the 45° sample in Figure 5b,e, the defect distribution is similar to that of the 0° sample, and more defects can be observed in the upper region. The maximum Feret diameter of the as-built sample was about 240  $\mu\text{m}$ , and that of the heat-treated one was about 500  $\mu\text{m}$ . The porosity increased along the build direction, as shown in Figure 5h. In the lower region, the porosity was less than 0.2%, while the porosity in the upper region was even larger than 1.0%.



The defects in the 90° samples showed a uniform distribution along the build direction, as shown in Figure 5c,f. As a result, the 90° sample showed more regular porosity curves, as shown in Figure 5i. The maximum Feret diameter in the 90° as-built sample was 187 µm, and its porosity along the build direction ranged from 0 to 0.5%. After annealing treatment, the maximum Feret diameter increased about four times to 730 µm, and the porosity increased by two times.

The porosity distribution along the build direction can be affected by cross-section changes in the AM metal parts, as shown in Figure 6. For the 0° sample and the 45° sample, the cross-section in the lower region increased along the build direction, as shown in Figure 6a,b. The input energy was transferred to the former region with a smaller area, and more energy could be used to heal the existing defects and reduce porosity. But in the upper region, the cross-section decreased along the build direction, and the energy was more diffusely transferred to the substrate material, thereby reducing defect healing and causing higher porosity. The defect-healing phenomenon was also observed by Chen [9]. For the 90° sample, the fixed cross-section can reduce the influential factor during LPBF and lead to a uniform distribution, as shown in Figure 6c.

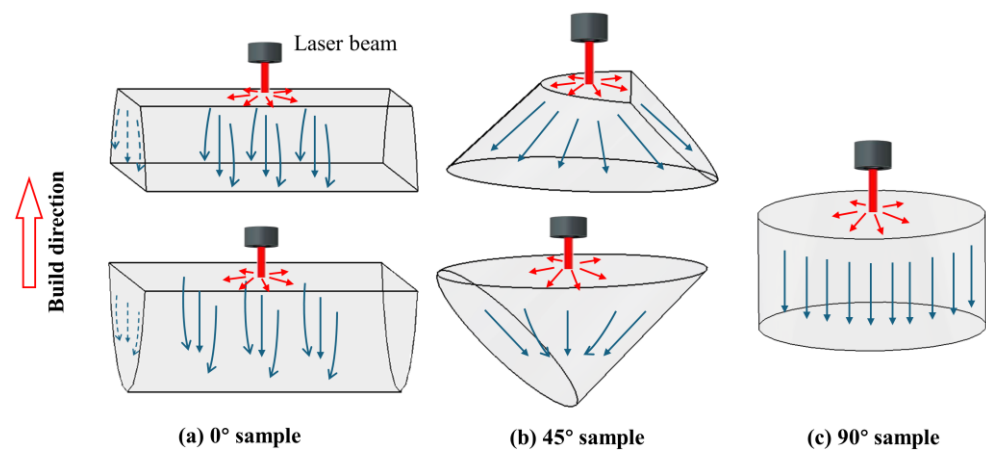


**Figure 6.** Cross-section gradient and heat transfer.

### 3.2.3. Defect Distribution along the Radial Direction

The defect position, especially its distance from the AM structural surface, can lead to different stress concentration factors, which subsequently affect the fatigue crack initiation site and fatigue strength. During printing, a higher cooling rate in the subsurface region can cause larger defects and higher porosity. So, all cylindrical samples were divided into ten regions along the radial direction. The porosities and defect distribution are shown in Figure 7.

The agglomeration of defects near cylindrical surfaces was observed in the 90° samples, as shown in Figure 7c,f. Additionally, the 0° sample and the 45° sample exhibited several large defects in the center region, and these defects can be observed at both ends of samples in Figure 7a,b,d,e separately. All samples had higher porosity in the subsurface region, which is about five times as high as those of other regions in the 0° sample and the 45° sample, and even more than ten times for the 90° sample shown in Figure 7f.

## 3.3. Defect Characterization

### 3.3.1. Defect Size

The maximum Feret diameter of internal defects of all samples was detected and is shown in Figure 8. The defect size shows the same distribution trend, and it can be fitted by a lognormal distribution function:

$$y = y_0 + \frac{A_0}{\sqrt{2\pi}wx} e^{-\frac{[\ln \frac{x}{x_0}]^2}{2w^2}} \quad (8)$$



where  $y_0$ ,  $xc$ ,  $w$  and  $A_0$  are constants, and the fitted values are listed in the table separately in Figure 8. After heat treatment, the defect size distribution curve of each sample was ‘flattened’ and ‘elongated’, that is, the peak of the curves decreased, and the abscissa corresponding to the peak was offset to the right, as shown in Figure 8a–c. Correspondingly, the proportion of small defects decreased, while the number of large defects increased after samples were heat-treated.

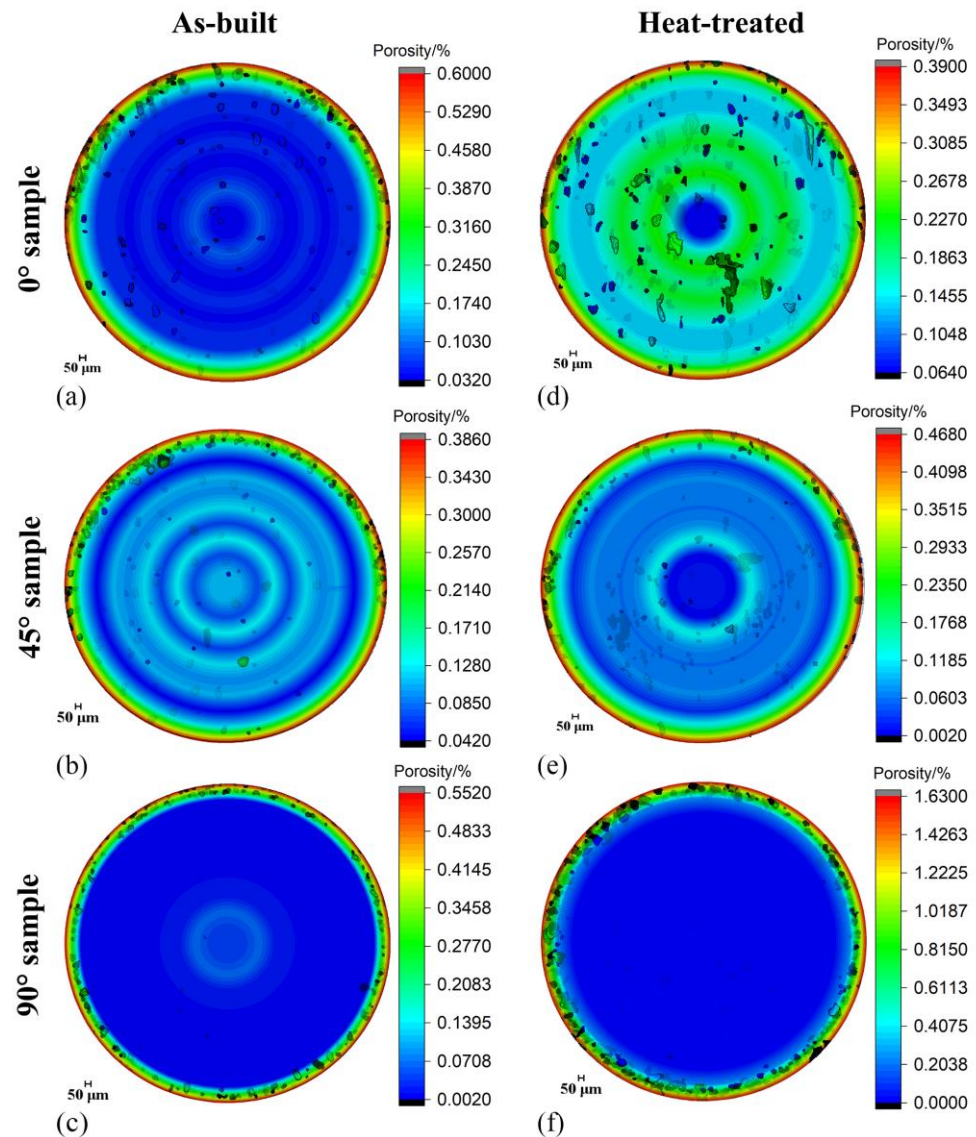


**Figure 7.** Defect along the radial direction and its porosity distribution: (a) the 0° as-built sample, (b) the 45° as-built sample, (c) the 90° as-built sample, (d) the 0° heat-treated sample, (e) the 45° heat-treated sample, (f) the 90° heat-treated sample.

The defect size distributions of the as-built samples in different build directions are compared and shown in Figure 8d. When the build direction increased, the proportion of small defects in the as-built samples also increased. The difference in contour scan and heat transfer in the subsurface region can lead to different quantity and size distributions of defects. The 90° sample with a radian contour shown in Figure 6c can produce more small defects, while the 0° sample has a small number of defects but a larger volume.

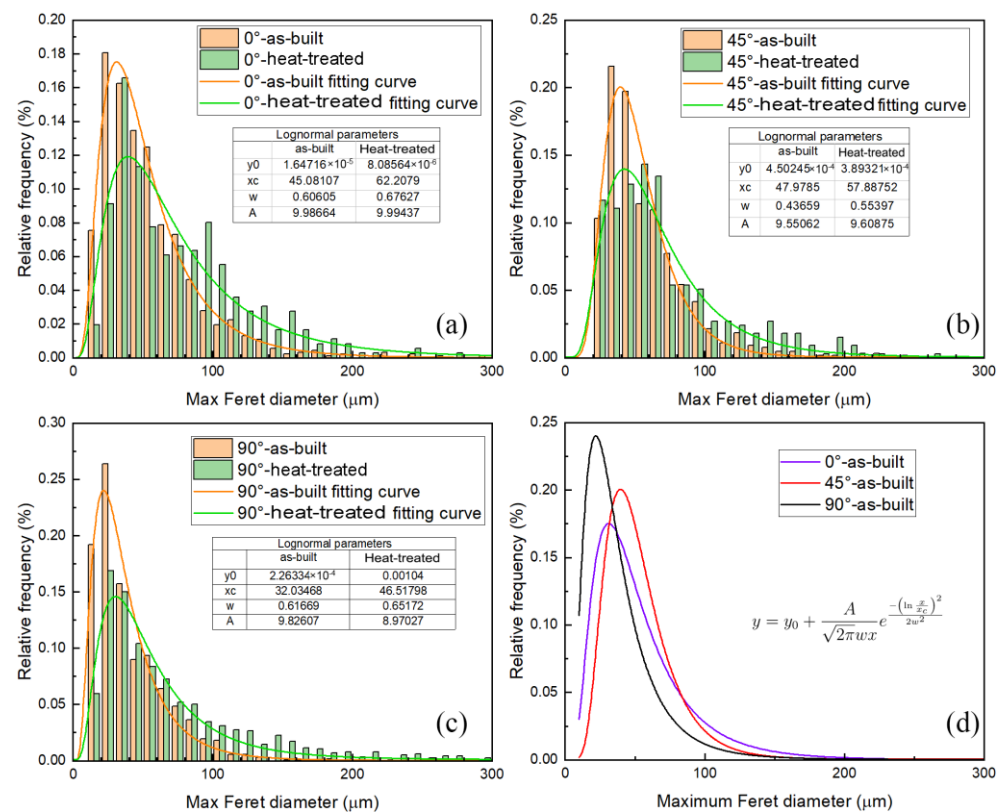


**Figure 8.** Defect size distribution in different build direction samples: (a) the 0° sample, (b) the 45° sample, (c) the 90° sample, (d) comparison of the as-built samples.

The build direction effect on defect size distribution shows the same tendency both in the as-built sample and the heat-treated sample. According to statistical results shown in Figure 8,  $y_0$  is very small and can be neglected, and  $A_0$  is independent of the build direction in Equation (8). So, the distribution can be expressed as the function related to the build direction  $\Theta$  (in degrees):

$$y = \frac{10}{\sqrt{2\pi}w(\Theta)x} e^{-\frac{[\ln \frac{x}{x_c(\Theta)}]^2}{2w(\Theta)^2}} \quad (9)$$

where  $w(\Theta) = 0.669 - 0.005 \times \Theta + 5.378 \times 10^{-5} \times \Theta^2$ ,  $x_c(\Theta) = 64.850 - 2.648 \times e^{0.022 \cdot \Theta}$ . The defect size distribution curves of the heat-treated samples can be well fitted by Equation (9), as shown in Figure 9.

### 3.3.2. The Sphericity

The sphericity  $\Psi$  is an efficient parameter to describe morphological characteristics of defects, and it can be calculated by the surface area  $A$  and volume  $V$  of the defect [10].

$$\Psi = \frac{6\pi^{\frac{1}{2}} \cdot V}{A^{\frac{3}{2}}} \quad (10)$$

The sphericity can be used to classify defect types, and its value ranges from 0 to 1. When  $\Psi$  reaches the maximum value of 1, the defect shows a perfectly spherical shape, while the morphology of a defect with a lower sphericity will show a concave, elongated, or irregular shape. It is generally believed that the defect with sphericity greater than 0.7 can be regarded as a pore, and that with a lower value is an LoF defect [10].

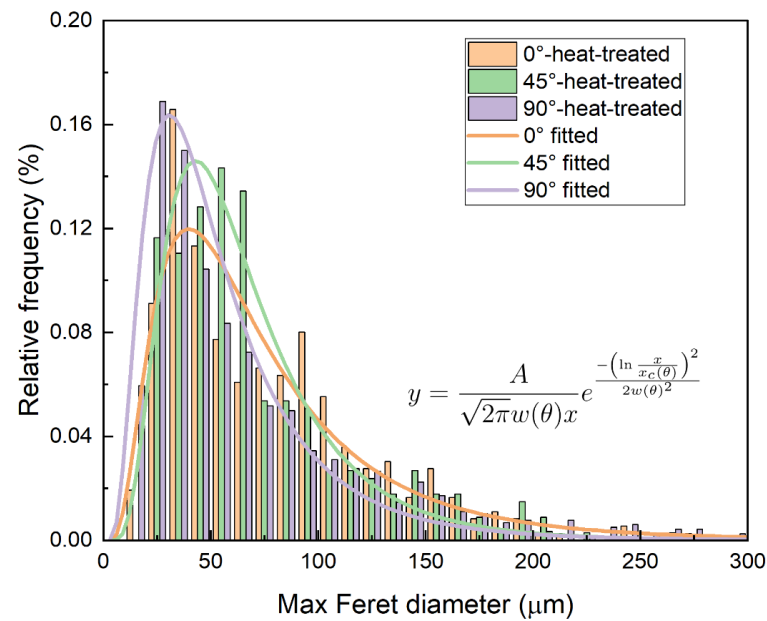


Figure 9. Defect size distribution of the heat-treated samples.

The distributions of sphericity in three build direction samples and the effect of heat treatment are plotted and compared, as shown in Figure 10.

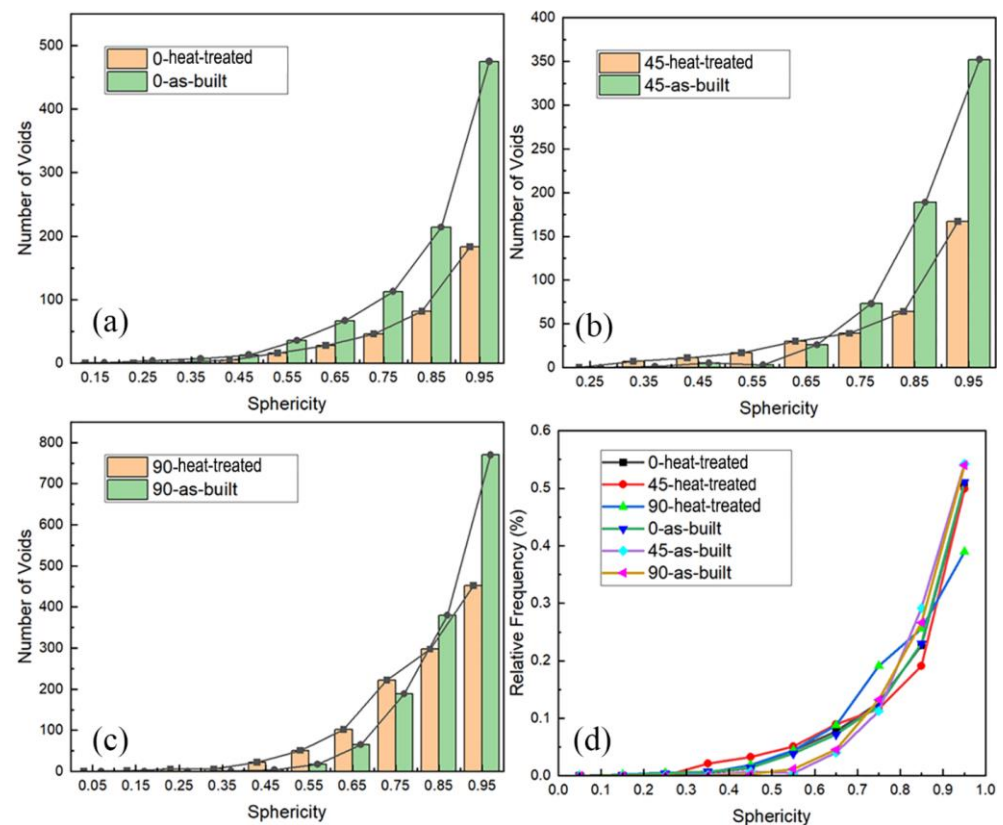


Figure 10. Sphericity distribution: (a) the 0° sample, (b) the 45° sample, (c) the 90° sample, (d) comparison of the fitted relative frequency curves.

A higher proportion of pore defects can be observed in three kinds of samples, whether the heat treatment was carried out or not. The sphericity distribution can be changed by

heat treatment, as shown in Figure 10a–c. The pore defect can coalesce into an elongated LoF defect under high-temperature conditions, and then a significant proportion decrease of the defect with a large sphericity occurs. The more pore defects, the more obvious the proportion change, especially in the 90° sample, as shown in Figure 10c. The fitted relative frequency curves of all samples are compared in Figure 10d, and it can be seen that the sphericity distribution is independent of build direction.

The probability distribution curves of sphericity can be fitted by a two-phase exponential growth function as follows:

$$y = y_1 + A_1 e^{\frac{x-x_0}{t_1}} + A_2 e^{\frac{x-x_0}{t_2}} \quad (11)$$

where  $x_0$ ,  $y_1$ ,  $A_1$ ,  $A_2$ ,  $t_1$  and  $t_2$  are constants. The fitted values are listed in Table 3, and all the R-square values are larger than 0.98.

**Table 3.** Sphericity distribution curve.

Types	Build Direction	Fitted Parameters						R-Square
		$x_0$	$y_1$	$A_1$	$A_2$	$t_1$	$t_2$	
As-built	0°	0.31995	−0.0032	$6.62282 \times 10^{-9}$	0.01062	0.03782	0.17359	0.99975
	45°	−0.03338	−0.00738	$2.36731 \times 10^{-4}$	$2.04758 \times 10^{-4}$	0.13768	0.13768	0.99426
	90°	−0.04092	−0.00615	$3.41384 \times 10^{-4}$	$8.86687 \times 10^{-5}$	0.13855	0.13855	0.99818
Heat-treated	0°	0.38115	−0.00621	$1.44019 \times 10^{-10}$	0.01877	0.0277	0.18715	0.99941
	45°	0.02805	0.01209	0.00231	−0.002	0.12565	0.12565	0.98283
	90°	−0.06787	−0.001701	0.00187	0.00364	0.23569	0.23568	0.98934

### 3.3.3. Defect Orientation and Aspect Ratio

The percentage of LoF defects ( $\Psi < 0.7$ ) cannot be neglected, which indicates that there are a lot of long and narrow defects with a large aspect ratio. The difference in defect orientation is of great significance to crack initiation and propagation. Therefore, the defect orientation is analyzed statistically. In Dragonfly, the defect orientation is determined by an eigenvector associated with the smallest eigenvalue of the inertia tensor, which represents the axis of the easiest rotation, and the long axis of the defect. The defect orientation in this section is defined as the angle between the major axis of the defect and the build direction, as shown in Figure 11. It means that the defects with a lower orientation are prone to distributing along the build direction, while the defects with a large orientation are distributed perpendicular to the build direction.

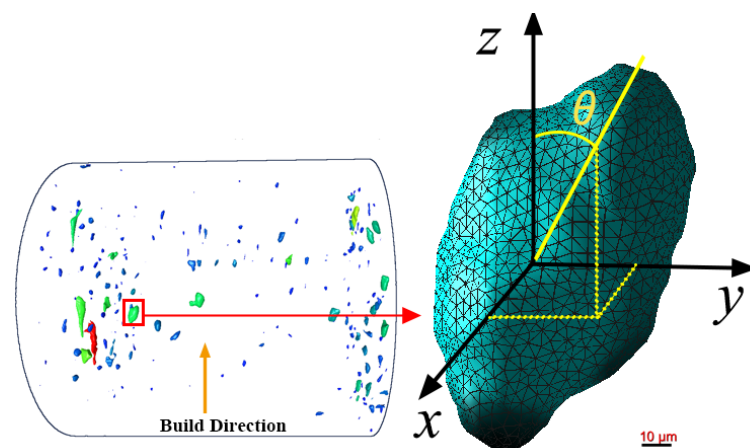


**Figure 11.** Defect orientation.

The relationship between defect orientation and build direction in LPBF Ti6Al4V titanium alloy, as well as the effect of heat treatment, is shown in Figure 12. The defect

orientation ranges from  $0^\circ$  to  $90^\circ$ , and the statistics are made on defects in each interval increment of  $10^\circ$ . The heat treatment effect and different distributions appeared in three build direction samples.

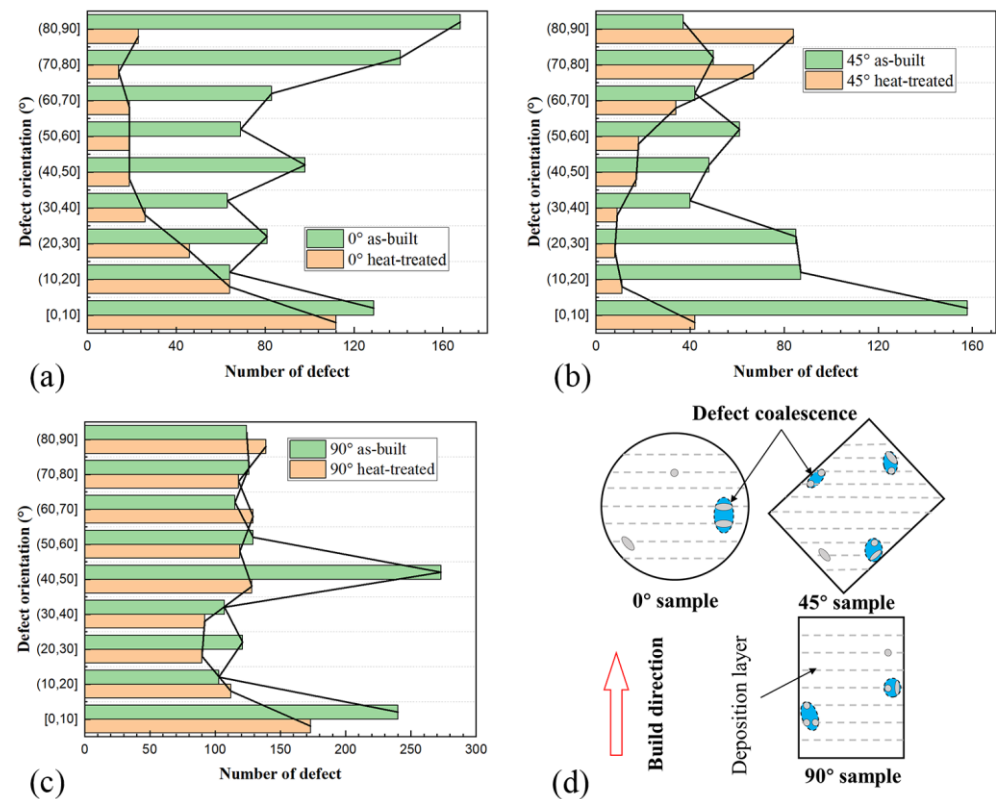


**Figure 12.** Defect orientation in different build direction samples: (a) the  $0^\circ$  sample, (b) the  $45^\circ$  sample, (c) the  $90^\circ$  sample, (d) defect coalescence under annealing treatment.

In Figure 12a, a reverse distribution is obvious for the  $0^\circ$  sample. The defects in the  $0^\circ$  as-built sample are mostly distributed along the scanning direction. After the heat treatment, the defect coalescence between adjacent layers leads to an increase in defect proportion along the build direction. The reason is that defects in the subsurface region are more likely to fuse along the axial direction of cylindrical samples under high temperatures, and then the defect orientation is deflected, as shown in Figure 12d.

A different distribution appeared in the  $45^\circ$  sample, as shown in Figure 12b. The tilt of the as-built sample made defects deflect along the cylindrical axial direction, and a higher proportion of small orientation defects were produced in the  $45^\circ$  as-built sample. After the heat treatment was performed, the defect coalescence along the build direction caused the reverse distribution. However, the defect orientation of the  $90^\circ$  sample exhibited a uniform distribution, as shown in Figure 12c, and it was not changed by the heat treatment.

The spatial characteristics of the defect can be fully described by the defect orientation, volume, and aspect ratio, and their relationships are shown in Figure 13. The aspect ratio is calculated as the ratio between the maximum Feret diameter and the minimum Feret diameter. There is no correlation between the aspect ratio and the defect volume. The aspect ratio is distributed from 1 to 4. After the samples were heat-treated, the aspect ratio and volume increased. It is worth noting that an alternate change in defect orientation with an increase in defect volume can be observed for all samples. Five regions were obtained according to the defect orientation ranges  $[0^\circ, 45^\circ)$  and  $[45^\circ, 90^\circ]$ , and the region can be visualized as the area delineated by grey and white stripes in Figure 13. In the region with the smallest or largest defect volume, the defect orientation is less than  $45^\circ$  and arranged in the build direction. The defect orientation will change continuously from the scanning



direction to the build direction, then to the scanning direction (as  $0^\circ$ – $45^\circ$ – $90^\circ$ – $45^\circ$ – $0^\circ$ ) with an increase in defect volume.

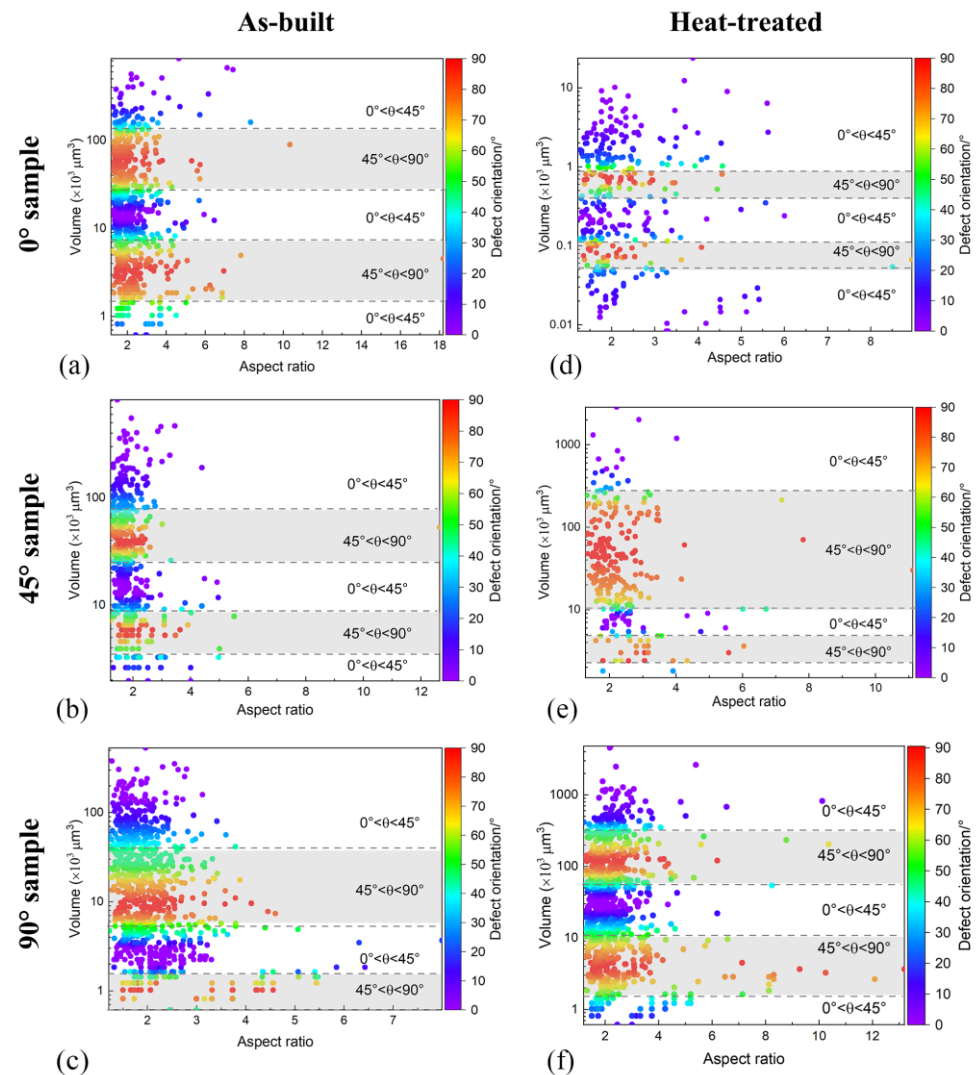


**Figure 13.** Volume–defect orientation–aspect ratio relationship: (a–c) the as-built sample in  $0^\circ$ ,  $45^\circ$ , and  $90^\circ$  build directions, (d–f) the heat-treated sample in  $0^\circ$ ,  $45^\circ$ , and  $90^\circ$  build directions.

### 3.4. Relationship between Defect and Fatigue Anisotropy

#### 3.4.1. The Equivalent Defect Size

The equivalent defect size is defined as the square root of the defect projected area,  $\sqrt{\text{area}}$ , on the cross-section of the tested sample (along the loading direction) in this study, and the irregularly projected shape of a single defect is regarded as an ellipse.  $\sqrt{\text{area}}$  and its distance from the sample surface of the  $0^\circ$  sample, the  $45^\circ$  sample, and the  $90^\circ$  sample are plotted in Figure 14. As the defect is distributed along the radial direction in Figure 7, the defect number decreases as the distance from the surface increases, which can also be clearly illustrated by the frequency curves of solid lines in Figure 14a–c. A large proportion of  $\sqrt{\text{area}}$  was less than  $150 \mu\text{m}$ , and the defect larger than  $80 \mu\text{m}$  was calculated and is shown in Figure 14d. After the heat treatment, the relative frequency of larger defects increases greatly, but there is still a linear relationship with build direction.

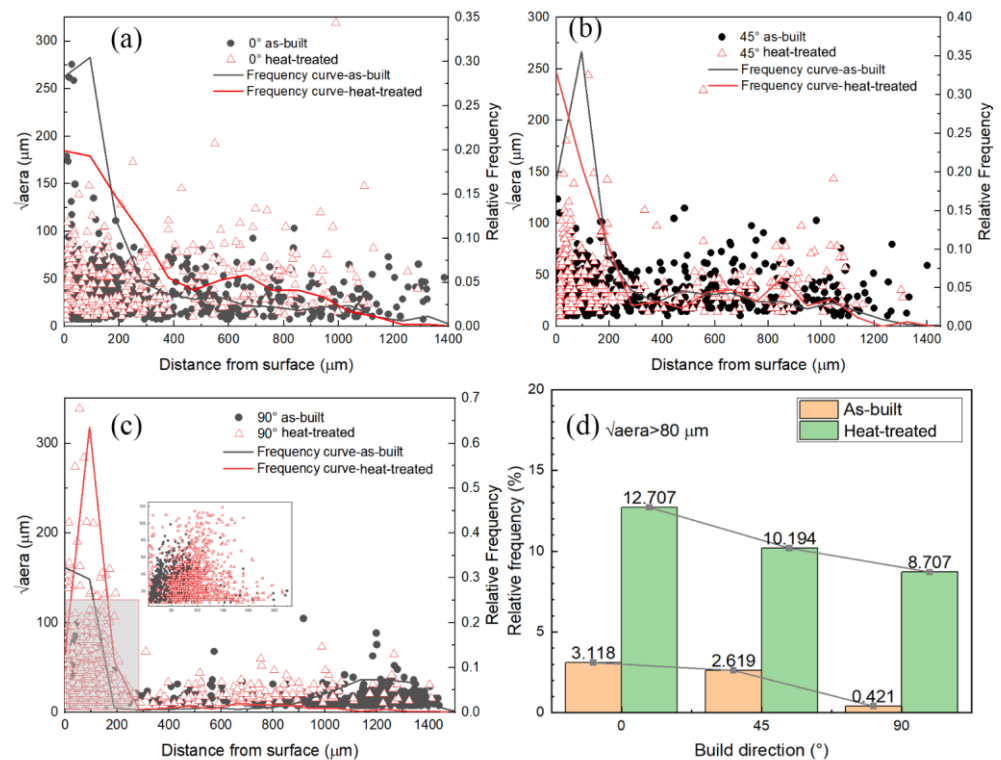


**Figure 14.**  $\sqrt{area}$  and its distance from the sample surface: (a) the 0° sample, (b) the 45° sample, (c) the 90° sample, (d) the relative frequency of large defects.

The spatial distribution of the effective equivalent defect size  $\sqrt{area_{eff}}$  of the heat-treated sample in 0°, 45°, and 90° build directions is plotted, and the orthogonal projection of defects along the loading direction is attached, as shown in Figure 15a–c separately. The sample starts cracking at the defect with a large  $\sqrt{area_{eff}}$  value, and it is mostly located in the subsurface region. Therefore, a surface machine treatment is necessary to enhance the fatigue life of AM alloys. To clarify this point, a smaller cylinder ( $\varnothing 2 \text{ mm} \times 1.5 \text{ mm}$ ) located in the central region of these three samples was extracted, and the defect was analyzed and is shown in Figure 15d–f separately. It can be found that both the defect number (or porosity) and the effective size of irregularly shaped defects were obtained, and  $\sqrt{area_{eff}}$  was reduced by more than four times from about 300  $\mu\text{m}$  to about 70  $\mu\text{m}$ .

### 3.4.2. Fatigue Anisotropy

In order to predict the size of the largest defect in the heat-treated samples, 10 regions with a 200  $\mu\text{m}$  depth along the loading direction were segmented for all samples. The relation between the reduced variate  $y$  and the extreme defect size  $\sqrt{area_{eff}}$  was fitted by linear curves, as shown in Figure 16. The build direction can affect the fatigue limit due to the change in the predicted maximum defect size. When the theoretical probability  $G(\sqrt{area_{eff}}) = 95\%$ , the estimations of effective defect size are calculated separately:  $\sqrt{area_{eff}/0^\circ} = 146 \mu\text{m}$ ,  $\sqrt{area_{eff}/45^\circ} = 182 \mu\text{m}$ ,  $\sqrt{area_{eff}/90^\circ} = 247 \mu\text{m}$ .

The relationship between the fatigue limit  $\sigma_w$  and the defect size  $\sqrt{area}$  is shown in Figure 17. As mentioned, cracks in AM alloy can initiate at a subsurface defect, and then the location factor  $C$  equals 1.43 in Equation (7). Finally, the fatigue limits are calculated:  $\sigma_w = 306 \text{ MPa}$ , 295 MPa, and 280 MPa for the 0° heat-treated sample, the 45° heat-treated sample, and the 90° heat-treated sample, respectively. It is shown that the different defect distributions related to the build direction can cause fatigue anisotropy of LPBF Ti6Al4V, and the fatigue limit decreases with the increase in the build direction.

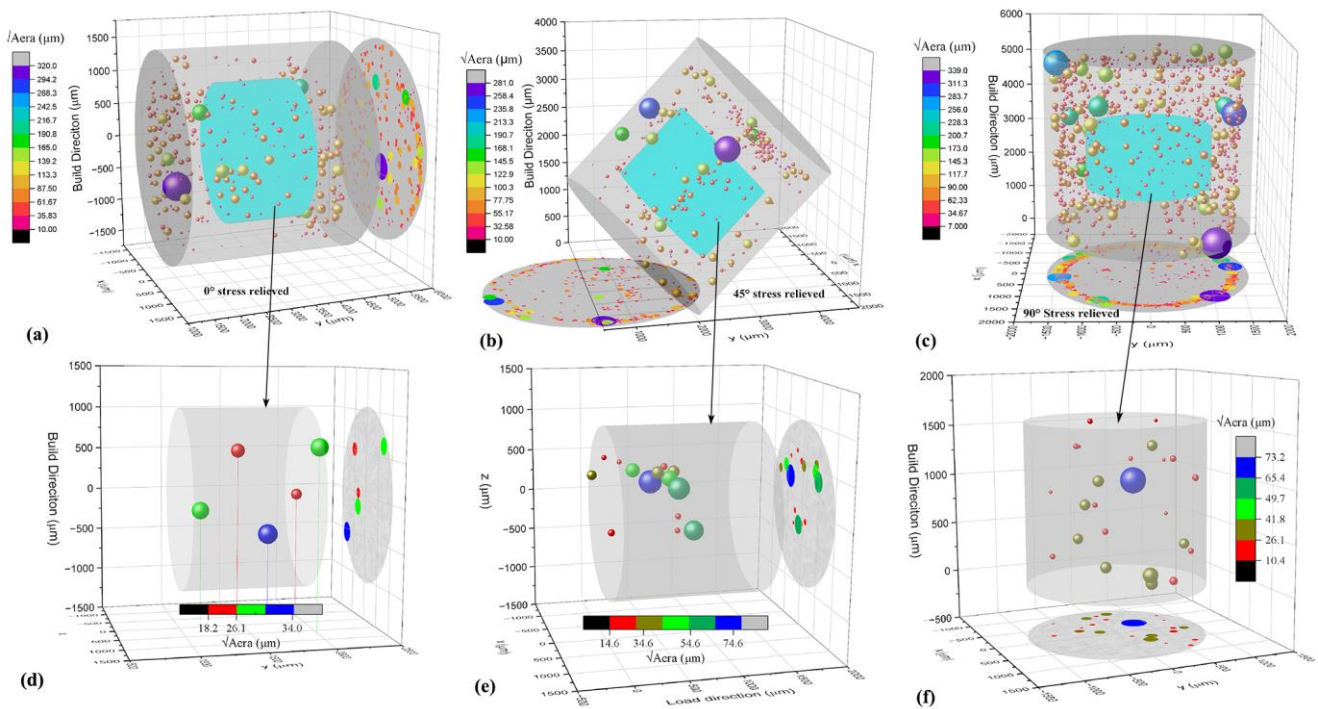


**Figure 15.**  $\sqrt{area_{eff}}$  distribution under the heat-treated condition: (a) the 0° sample, (b) the 45° sample, (c) the 90° sample, (d–f) the heartland of the 0° sample, 45° sample, and 90° sample.

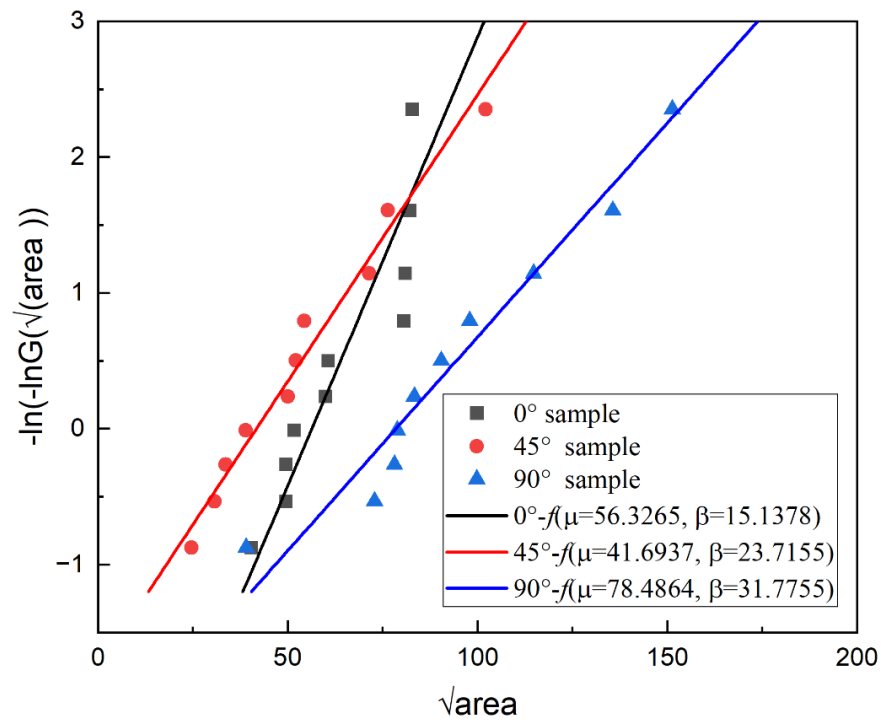


**Figure 16.** Statistics of extremes of defects in heat-treated samples.

After the sample surface was machined,  $\sqrt{area_{eff}}$  in the 90° heat-treated sample was reduced to about 70  $\mu\text{m}$ , with an approximate corresponding fatigue limit of 350 MPa. This prediction is well matched with our previous experimental data [60,61].

### 3.4.3. Effect of Defect Characteristics

Defects can cause a higher stress concentration, which is the primary cause of crack initiation. The position, orientation, and aspect ratio of defects can affect the stress concentration factor  $K_t$ . Meanwhile,  $\sqrt{\text{area}}$  is the main parameter in the Murakami equation in Equation (7), and it did not take the defect position, orientation, and aspect ratio into consideration. Hence, the contribution of defect characteristics to the fatigue limit of LPBF Ti6Al4V alloys is missed.

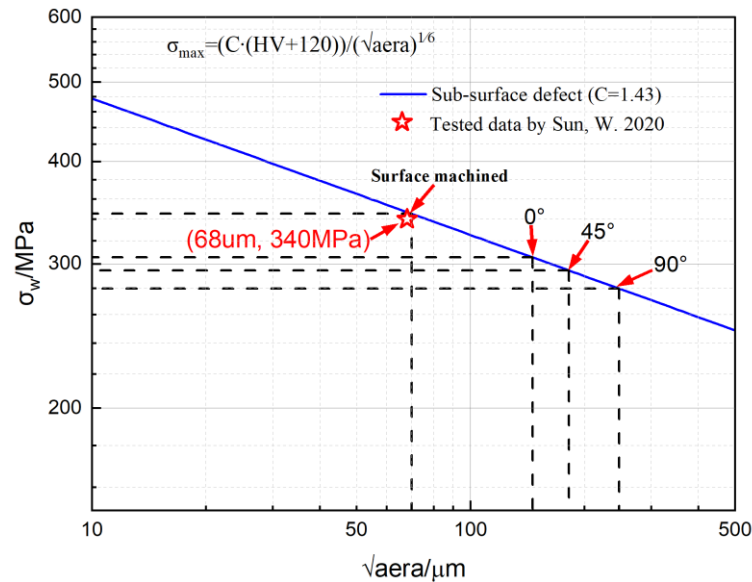


Figure 17. Relationship between fatigue limit and  $\sqrt{\text{area}}$  [60].

The  $\sqrt{\text{area}_{eff}}$  was calculated firstly by the projected area of the defect along the loading direction. It should be noted that the same  $\sqrt{\text{area}_{eff}}$  can be obtained by different types of defects 1#, 2#, and 3#, as shown in Figure 18a. The defect characteristic effect was simulated by the finite element method (FEM), and the results are shown in Figure 18b–d.

Finite element models of samples with different defects were built in ABAQUS software (Version 2017) and are shown in Figure 18. The C3D10 quadratic tetrahedron element was used, and the minimum mesh size around the defect was 10  $\mu\text{m}$  after the converged mesh was verified. The normalized distance  $\delta$  was defined as the ratio of the distance of  $d$  from the free surface to the radius  $\Phi$  of the cylinder. It was shown that these three defects, with the same value of the projected area (1#, 2#, and 3# in Figure 18a), indeed cause different  $K_t$ . Figure 18b shows that  $K_t$  decays exponentially with increasing  $\delta$ ,

$$f(\delta) = 0.868 + 2.406 \times e^{-14.531 \times \delta} \quad (12)$$

The stress concentration becomes greater with the increase in defect orientation  $\theta$  and defect aspect ratio  $r$ , as shown in Figure 18c,d. The normalized  $K_t$  was fitted with Equations (13) and (14).

$$f(\theta) = 0.608 + 0.009 \times \theta \quad (13)$$

$$f(r) = 0.773 \times r^{0.192} \quad (14)$$

If the projected area was used to replace the spatial defect in the Murakami model, a reduction factor related to the normalized  $K_t$  should be considered in the estimations, and the extended effective defect size  $\sqrt{\text{area}_{eff}^{EXTD}}$  can be expressed.

$$\sqrt{\text{area}_{eff}^{EXTD}} = g(\delta, \theta, r) \cdot \sqrt{\text{area}_{eff}} \quad (15)$$

where the function  $g(\delta, \theta, r)$  can be calculated by Equation (16).

$$g(\delta, \theta, r) = f(\delta) \cdot f(\theta) \cdot f(r) \quad (16)$$

and  $f(\delta)$ ,  $f(\theta)$  and  $f(r)$  can be obtained by Equations (12)–(14). Thus,  $\sqrt{area_{eff}}^{EXTD}$  indicated by the filled circles were compared with their original values indicated by the hollow circles, as shown in Figure 19. It was observed that both the maximum  $\sqrt{area_{eff}}$  value and fatigue crack initiation sites in three kinds of samples were changed, and the distributions are shown in Figure 19a–c. The estimated  $\sqrt{area_{eff}}$  reduced to 111  $\mu\text{m}$ , 149  $\mu\text{m}$ , and 204  $\mu\text{m}$  for the 0° heat-treated sample, the 45° heat-treated sample, and the 90° heat-treated sample, respectively. When the real defects in the 90° heat-treated sample were extracted to an FEM model, the stress distribution was obtained and is shown in Figure 19d. It shows that the crack initiation site obtained by the FEM model is identical to that predicted by  $\sqrt{area_{eff}}^{EXTD}$ .  $\sqrt{area_{eff}}^{EXTD}$  can be better used to predict the fatigue limit of the LPBF Ti6Al4V alloy than the original  $\sqrt{area_{eff}}$ .

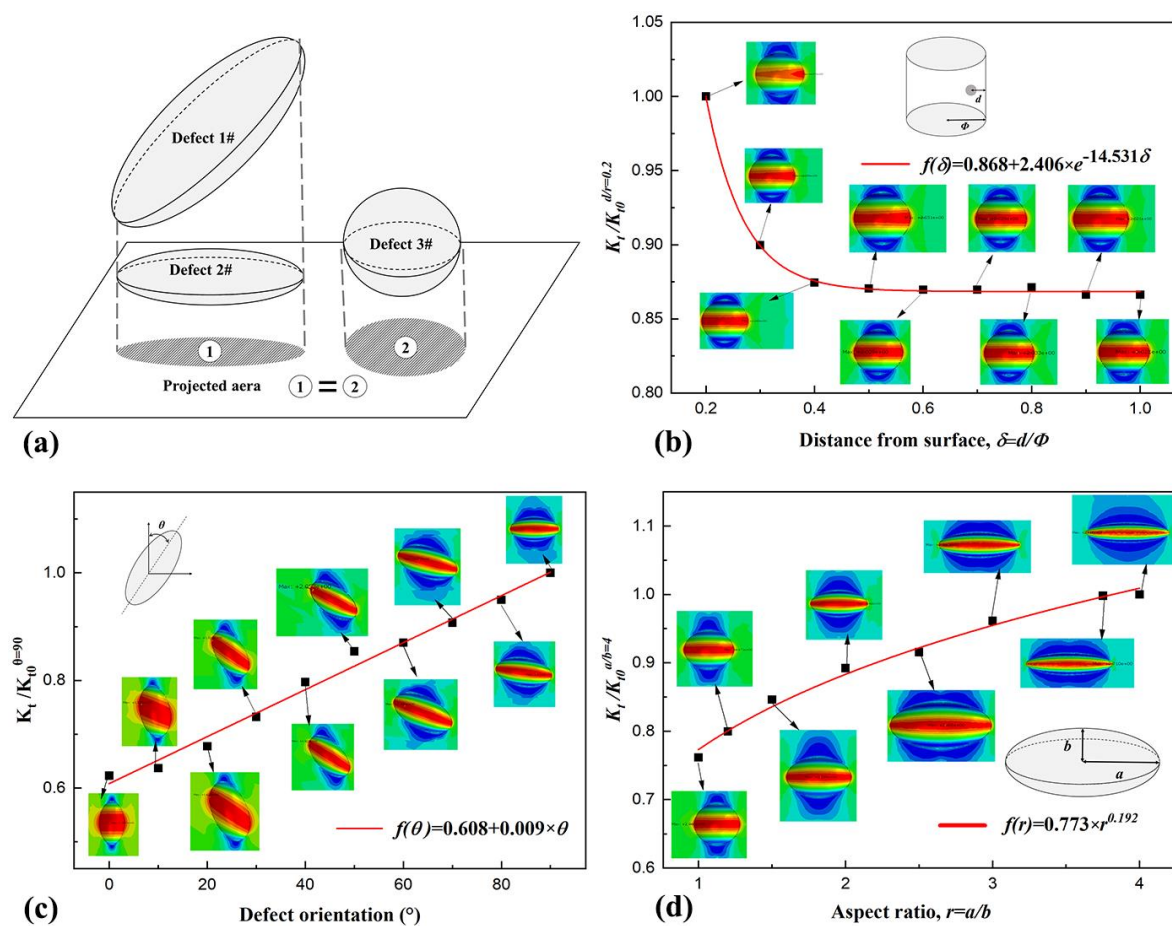


**Figure 18.** Effect of the defect characteristics on stress concentration: (a) defect with the same projected area, (b) position, (c) orientation, (d) aspect ratio.



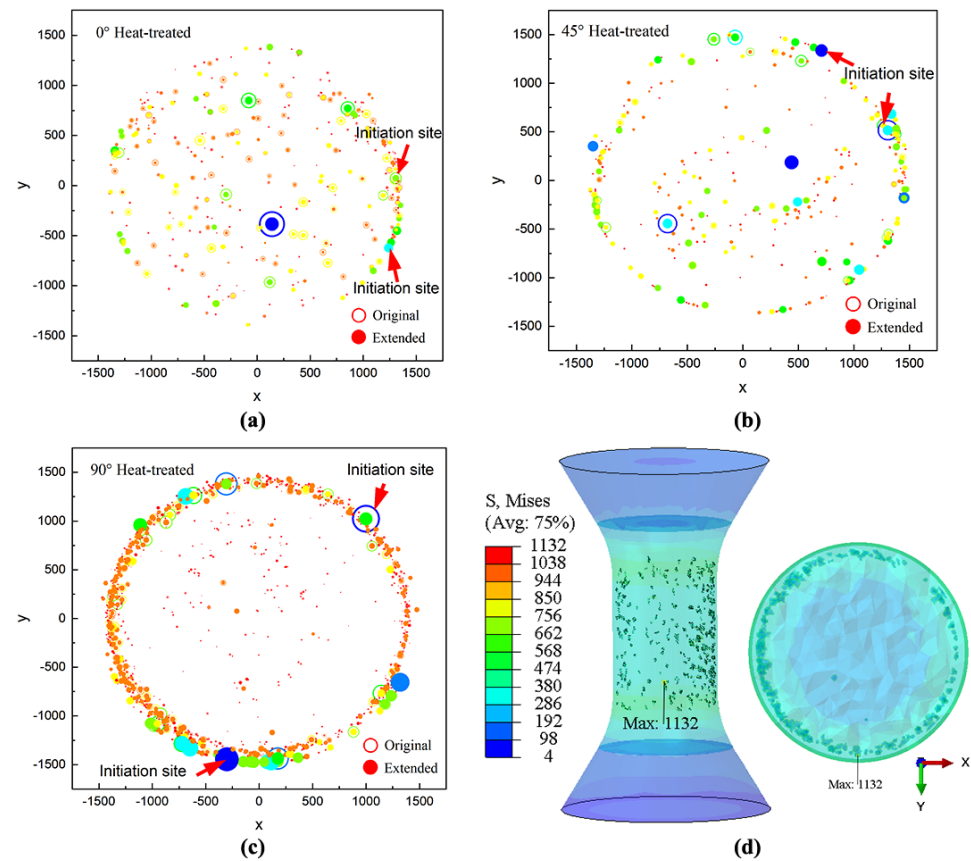


**Figure 19.** The  $\sqrt{area}$  distribution of heat-treated samples: (a) the 0° sample, (b) the 45° sample, (c) the 90° sample, (d) stress distribution with real defects in the 90° sample.

#### 4. Conclusions and Outlook

In this study, the spatial distribution of defects in LPBF Ti6Al4V titanium alloy was characterized. The effects of build direction and heat treatment were analyzed, and the main conclusions are as follows:

- (1) The build direction can affect the porosity distribution and the maximum defect size, while annealing treatment can cause the coalescence of small defects and higher porosity. For the as-built samples, the 0° sample exhibits the largest porosity of 0.18%, and it was 18.4% and 66.7% higher than the 45° sample and the 90° sample, respectively. After annealing treatment, the porosity of the 0° sample and the 45° sample increased slightly, while that of the 90° sample increased more than three times.
- (2) Larger defects are prone to present in the consecutive deposition layers, and the subsurface region exhibits significantly higher porosity compared to other regions. The defect size obeys a lognormal distribution, and the sphericity can be fitted by a two-phase exponential growth function.
- (3) The defect orientation is related to the build direction and can be changed by heat treatment. The defect orientation is related to its volume, and the defect orientation alternately changed in the order of 0°–45°–90°–45°–0° with the increase in defect volume.
- (3) Different defect distributions, resulting from build direction, can lead to anisotropic fatigue performance. An extended effective defect size  $\sqrt{area_{eff}}^{EXTD}$  considering its position, orientation, and aspect ratio was successfully used in the Murakami model. The predicted fatigue limit was in good agreement with the experiment results.

In future investigations, the coupled effects of microstructure and defects on fatigue anisotropy and the parametric characterization method will be investigated. In addition, the

size effect on defect distribution and a processing parameter-dependent fatigue prediction of failure defects will be determined.

**Author Contributions:** Conceptualization, W.S. and Y.M.; validation, P.L., Z.M., and W.Z.; formal analysis, W.S. and P.L.; investigation, Y.M. and P.L.; data curation, W.S.; writing—original draft preparation, W.S.; writing—review and editing, Y.M. and Z.M.; visualization, W.S.; supervision, Y.M. and W.Z.; project administration, W.Z.; funding acquisition, W.S., Y.M., and W.Z. All authors have read and agreed to the published version of the manuscript.

**Funding:** This study was financially supported by the National Natural Science Foundation of China under Grant No. 12302103, No. 12032018, and No. U2341238.

**Data Availability Statement:** The raw data supporting the conclusions of this article will be made available by the authors on request.

**Conflicts of Interest:** The authors declare no conflicts of interest. The funders had no role in the design of the study; in the collection, analyses, or interpretation of data; in the writing of the manuscript; or in the decision to publish the results.

## References

- Joshi, K.; Promoppatum, P.; Quek, S.S.; Raghavan, S.; Johan, N.S.; Shukla, S.; Samudrala, S.; van der Veen, S.; Jhon, M.H. Effect of porosity distribution on the strength and strain-to-failure of Laser Powder Bed Fusion printed Ti-6Al-4V. *Addit. Manuf.* **2023**, *75*, 103738. [\[CrossRef\]](#)
- Siddiqui, S.F.; Araiza, E. Microstructural defects governing torsional fatigue failure of additively manufactured as-built and heat-treated Inconel 718. *Eng. Fail. Anal.* **2023**, *144*, 106975. [\[CrossRef\]](#)
- du Plessis, A.; Yadroitsava, I.; Yadroitsev, I. Effects of defects on mechanical properties in metal additive manufacturing: A review focusing on X-ray tomography insights. *Mater. Des.* **2020**, *187*, 108385. [\[CrossRef\]](#)
- Li, H.; Tian, Z.; Zheng, J.; Huang, K.; Nie, B.; Xu, W.; Zhao, Z. A defect-based fatigue life estimation method for laser additive manufactured Ti-6Al-4V alloy at elevated temperature in very high cycle regime. *Int. J. Fatigue* **2023**, *167*, 107375. [\[CrossRef\]](#)
- Hu, D.; Pan, J.; Mi, D.; Mao, J.; Li, W.; Fu, Y.; Wang, R. Prediction of anisotropic LCF behavior for SLM Ti-6Al-4V considering the spatial orientation of defects. *Int. J. Fatigue* **2022**, *158*, 106734. [\[CrossRef\]](#)
- Sanaei, N.; Fatemi, A. Analysis of the effect of internal defects on fatigue performance of additive manufactured metals. *Mater. Sci. Eng. A* **2020**, *785*, 139385. [\[CrossRef\]](#)
- Cunningham, R.; Narra, S.P.; Ozturk, T.; Beuth, J.; Rollett, A.D. Evaluating the Effect of Processing Parameters on Porosity in Electron Beam Melted Ti-6Al-4V via Synchrotron X-ray Microtomography. *JOM* **2016**, *68*, 765–771. [\[CrossRef\]](#)
- Wang, J.; Cui, Y.; Liu, C.; Li, Z.; Wu, Q.; Fang, D. Understanding internal defects in Mo fabricated by wire arc additive manufacturing through 3D computed tomography. *J. Alloys Compd.* **2020**, *840*, 155753. [\[CrossRef\]](#)
- Chen, X.; Liao, W.; Yue, J.; Liu, T.; Zhang, K.; Li, J.; Yang, T.; Liu, H.; Wei, H. Unveiling the layer-wise dynamics of defect evolution in laser powder bed fusion: Insights for in-situ monitoring and control. *Addit. Manuf.* **2024**, *94*, 104414. [\[CrossRef\]](#)
- Kasperovich, G.; Haubrich, J.; Gussone, J.; Requena, G. Correlation between porosity and processing parameters in TiAl6V4 produced by selective laser melting. *Mater. Des.* **2016**, *105*, 160–170. [\[CrossRef\]](#)
- Xie, C.; Wu, S.; Yu, Y.; Zhang, H.; Hu, Y.; Zhang, M.; Wang, G. Defect-correlated fatigue resistance of additively manufactured Al-Mg4.5Mn alloy with in situ micro-rolling. *J. Mech. Work. Technol.* **2021**, *291*, 117039. [\[CrossRef\]](#)
- Mian, J.; Razmi, J.; Ladani, L. Defect analysis and fatigue strength prediction of as-built Ti6Al4V parts, produced using electron beam melting (EBM) AM technology. *Materialia* **2021**, *16*, 101041. [\[CrossRef\]](#)
- Qian, W.; Wu, S.; Wu, Z.; Ahmed, S.; Zhang, W.; Qian, G.; Withers, P.J. In situ X-ray imaging of fatigue crack growth from multiple defects in additively manufactured AlSi10Mg alloy. *Int. J. Fatigue* **2022**, *155*, 106616. [\[CrossRef\]](#)
- Liu, W.; Chen, C.; Shuai, S.; Zhao, R.; Liu, L.; Wang, X.; Hu, T.; Xuan, W.; Li, C.; Yu, J.; et al. Study of pore defect and mechanical properties in selective laser melted Ti6Al4V alloy based on X-ray computed tomography. *Mater. Sci. Eng. A* **2020**, *797*, 139981. [\[CrossRef\]](#)
- Malashin, I.; Martysyuk, D.; Tynchenko, V.; Evsyukov, D.; Nelyub, V.; Borodulin, A.; Gantimurov, A.; Galinovsky, A. Predicting defects in SLM-produced parts based on melt pools clustering analysis. *Int. J. Adv. Manuf. Technol.* **2024**, *134*, 1169–1178. [\[CrossRef\]](#)
- Du, L.; Qian, G.; Zheng, L.; Hong, Y. Influence of processing parameters of selective laser melting on high-cycle and very-high-cycle fatigue behaviour of Ti-6Al-4V. *Fatigue Fract. Eng. Mater. Struct.* **2021**, *44*, 240–256. [\[CrossRef\]](#)
- Childerhouse, T.; Hernández-Nava, E.; Tapoglou, N.; M'saoubi, R.; Franca, L.; Leahy, W.; Jackson, M. The influence of finish machining depth and hot isostatic pressing on defect distribution and fatigue behaviour of selective electron beam melted Ti-6Al-4V. *Int. J. Fatigue* **2021**, *147*, 106169. [\[CrossRef\]](#)
- Sanaei, N.; Fatemi, A. Defects in additive manufactured metals and their effect on fatigue performance: A state-of-the-art review. *Prog. Mater. Sci.* **2021**, *117*, 100724. [\[CrossRef\]](#)

19. Ng, C.; Bermingham, M.; Dargusch, M. Eliminating segregation defects during additive manufacturing of high strength  $\beta$ -titanium alloys. *Addit. Manuf.* **2021**, *39*, 101855. [\[CrossRef\]](#)
20. Moran, T.P.; Warner, D.H.; Phan, N. Scan-by-scan part-scale thermal modelling for defect prediction in metal additive manufacturing. *Addit. Manuf.* **2021**, *37*, 101667. [\[CrossRef\]](#)
21. Bartlett, J.L.; Jarama, A.; Jones, J.; Li, X. Prediction of microstructural defects in additive manufacturing from powder bed quality using digital image correlation. *Mater. Sci. Eng. A* **2020**, *794*, 140002. [\[CrossRef\]](#)
22. Hauser, T.; Reisch, R.T.; Breese, P.P.; Lutz, B.S.; Pantano, M.; Nalam, Y.; Bela, K.; Kamps, T.; Volpp, J.; Kaplan, A.F. Porosity in wire arc additive manufacturing of aluminium alloys. *Addit. Manuf.* **2021**, *41*, 101993. [\[CrossRef\]](#)
23. Bonneric, M.; Brugger, C.; Saintier, N. Effect of hot isostatic pressing on the critical defect size distribution in AlSi7Mg0.6 alloy obtained by selective laser melting. *Int. J. Fatigue* **2020**, *140*, 105797. [\[CrossRef\]](#)
24. Bustillos, J.; Kim, J.; Moridi, A. Exploiting lack of fusion defects for microstructural engineering in additive manufacturing. *Addit. Manuf.* **2021**, *48*, 102399. [\[CrossRef\]](#)
25. Seifi, M.; Salem, A.A.; Satko, D.P.; Ackelid, U.; Semiatin, S.L.; Lewandowski, J.J. Effects of HIP on microstructural heterogeneity, defect distribution and mechanical properties of additively manufactured EBM Ti-48Al-2Cr-2Nb. *J. Alloys Compd.* **2017**, *729*, 1118–1135. [\[CrossRef\]](#)
26. Poudel, A.; Yasin, M.S.; Ye, J.; Liu, J.; Vinel, A.; Shao, S.; Shamsaei, N. Feature-based volumetric defect classification in metal additive manufacturing. *Nat. Commun.* **2022**, *13*, 1–12. [\[CrossRef\]](#)
27. Hu, Y.N.; Wu, S.C.; Wu, Z.K.; Zhong, X.L.; Ahmed, S.; Karabal, S.; Xiao, X.H.; Zhang, H.O.; Withers, P.J. A new approach to correlate the defect population with the fatigue life of selective laser melt-ed Ti-6Al-4V alloy. *Int. J. Fatigue* **2020**, *136*, 105584. [\[CrossRef\]](#)
28. Yamashita, Y.; Murakami, T.; Mihara, R.; Okada, M.; Murakami, Y. Defect analysis and fatigue design basis for Ni-based super-alloy 718 manufactured by selective laser melting. *Int. J. Fatigue* **2018**, *117*, 485–495. [\[CrossRef\]](#)
29. Zhang, K.; Meng, Q.; Cai, N.; Qu, Z.; He, R. Effects of solid loading on stereolithographic additive manufactured ZrO<sub>2</sub> ceramic: A quantitative defect study by X-ray computed tomography. *Ceram. Int.* **2021**, *47*, 24353–24359. [\[CrossRef\]](#)
30. Hu, Y.; Wu, S.; Withers, P.; Zhang, J.; Bao, H.; Fu, Y.; Kang, G. The effect of manufacturing defects on the fatigue life of selective laser melted Ti-6Al-4V structures. *Mater. Des.* **2020**, *192*, 108708. [\[CrossRef\]](#)
31. Wu, Z.; Wu, S.; Bao, J.; Qian, W.; Karabal, S.; Sun, W.; Withers, P.J. The effect of defect population on the anisotropic fatigue resistance of AlSi10Mg alloy fabricated by laser powder bed fusion. *Int. J. Fatigue* **2021**, *151*, 106317. [\[CrossRef\]](#)
32. Hu, D.; Pan, J.; Mao, J.; Hu, S.; Liu, X.; Fu, Y.; Wang, R. Mechanical behavior prediction of additively manufactured components based on defect evolution observation by synchrotron radiation X-ray tomography. *Mater. Des.* **2021**, *198*, 109353. [\[CrossRef\]](#)
33. Seifi, M.; Salem, A.; Satko, D.; Shaffer, J.; Lewandowski, J.J. Defect distribution and microstructure heterogeneity effects on fracture resistance and fatigue behavior of EBM Ti-6Al-4V. *Int. J. Fatigue* **2017**, *94*, 263–287. [\[CrossRef\]](#)
34. Ge, J.; Ma, T.; Han, W.; Yuan, T.; Jin, T.; Fu, H.; Xiao, R.; Lei, Y.; Lin, J. Thermal-induced microstructural evolution and defect distribution of wire-arc additive manufacturing 2Cr13 part: Numerical simulation and experimental characterization. *Appl. Therm. Eng.* **2019**, *163*, 114335. [\[CrossRef\]](#)
35. Haridas, R.S.; Thapliyal, S.; Agrawal, P.; Mishra, R.S. Defect-based probabilistic fatigue life estimation model for an additively manufactured aluminum alloy. *Mater. Sci. Eng. A* **2020**, *798*, 140082. [\[CrossRef\]](#)
36. Romano, S.; Abel, A.; Gumpinger, J.; Brandão, A.; Beretta, S. Quality control of AlSi10Mg produced by SLM: Metallography versus CT scans for critical defect size assessment. *Addit. Manuf.* **2019**, *28*, 394–405. [\[CrossRef\]](#)
37. Xu, Z.; Liu, A.; Wang, X.; Liu, B.; Guo, M. Fatigue limit prediction model and fatigue crack growth mechanism for selective laser melting Ti6Al4V samples with inherent defects. *Int. J. Fatigue* **2021**, *143*, 106008. [\[CrossRef\]](#)
38. Bao, J.; Wu, S.; Withers, P.J.; Wu, Z.; Li, F.; Fu, Y.; Sun, W. Defect evolution during high temperature tension-tension fatigue of SLM AlSi10Mg alloy by synchrotron tomography. *Mater. Sci. Eng. A* **2020**, *792*, 139809. [\[CrossRef\]](#)
39. Cao, S.; Zhang, H.; Hu, J.; Li, C.; Li, B. Fatigue life prediction model for shot-peened laser powder bed fused 304L steel considering residual stress relaxation and defect distribution. *Eng. Fail. Anal.* **2024**, *162*, 108423. [\[CrossRef\]](#)
40. Li, W.; Song, P.; Sun, C.; Zhang, Y. Defect induced fatigue failure behavior and life assessment of laser powder bed fused Al-Si alloy under different building directions. *Eng. Fail. Anal.* **2024**, *156*, 107826. [\[CrossRef\]](#)
41. Biswal, R.; Syed, A.K.; Zhang, X. Assessment of the effect of isolated porosity defects on the fatigue performance of additive manufactured titanium alloy. *Addit. Manuf.* **2018**, *23*, 433–442. [\[CrossRef\]](#)
42. Biswal, R.; Zhang, X.; Syed, A.K.; Awd, M.; Ding, J.; Walther, F.; Williams, S. Criticality of porosity defects on the fatigue performance of wire + arc additive manufactured titanium alloy. *Int. J. Fatigue* **2019**, *122*, 208–217. [\[CrossRef\]](#)
43. Liu, B.; Chen, B.; Lu, S.; Wang, Q.; Bao, R. Investigations into Gas-Pore Effects on Fatigue Strength with a Peridynamic Approach. *Aerospace* **2022**, *9*, 641. [\[CrossRef\]](#)
44. Akgun, E.; Zhang, X.; Biswal, R.; Zhang, Y.; Doré, M. Fatigue of wire+arc additive manufactured Ti-6Al-4V in presence of process-induced porosity defects. *Int. J. Fatigue* **2021**, *150*, 106315. [\[CrossRef\]](#)
45. Rotella, A.; Nadot, Y.; Piellard, M.; Augustin, R.; Fleuriot, M. Influence of defect morphology and position on the fatigue limit of cast Al alloy: 3D characterization by X-ray microtomography of natural and artificial defects. *Mater. Sci. Eng. A* **2020**, *785*, 139347. [\[CrossRef\]](#)

46. Luo, Y.; Zhang, B.; Feng, X.; Song, Z.; Qi, X.; Li, C.; Chen, G.; Zhang, G. Pore-affected fatigue life scattering and prediction of additively manufactured Inconel 718: An investigation based on miniature specimen testing and machine learning approach. *Mater. Sci. Eng. A* **2021**, *802*, 140693. [\[CrossRef\]](#)
47. Prithivirajan, V.; Sangid, M.D. The role of defects and critical pore size analysis in the fatigue response of additively manufactured IN718 via crystal plasticity. *Mater. Des.* **2018**, *150*, 139–153. [\[CrossRef\]](#)
48. Shamir, M.; Syed, A.K.; Janik, V.; Biswal, R.; Zhang, X. The role of microstructure and local crystallographic orientation near porosity defects on the high cycle fatigue life of an additive manufactured Ti-6Al-4V. *Mater. Charact.* **2020**, *169*, 110576. [\[CrossRef\]](#)
49. Yeratapally, S.R.; Lang, C.; Glaessgen, E.H. A computational study to investigate the effect of defect geometries on the fatigue crack driving forces in powder-bed AM materials. In Proceedings of the AIAA Scitech 2020 Forum, Orlando, FL, USA, 6–10 January 2020.
50. Dunstan, M.K.; Paramore, J.D.; Fang, Z.Z. The effects of microstructure and porosity on the competing fatigue failure mechanisms in powder metallurgy Ti-6Al-4V. *Int. J. Fatigue* **2018**, *116*, 584–591. [\[CrossRef\]](#)
51. Zou, J.; Xia, X.; Feng, Z.; Wang, J.; Guo, Y.; Gao, D. The fatigue mechanism and a new defect-based life prediction model for selective laser melted Al-Mg-Sc-Zr alloy. *Int. J. Fatigue* **2024**, *190*, 108590. [\[CrossRef\]](#)
52. Afazov, S.; Serjouei, A.; Hickman, G.J.; Mahal, R.; Goy, D.; Mitchell, I. Defect-based fatigue model for additive manufacturing. *Prog. Addit. Manuf.* **2023**, *8*, 1059–1066. [\[CrossRef\]](#)
53. Nadot, Y. Fatigue from Defect: Influence of Size, Type, Position, Morphology and Loading. *Int. J. Fatigue* **2022**, *154*, 106531. [\[CrossRef\]](#)
54. Teschke, M.; Moritz, J.; Tenkamp, J.; Marquardt, A.; Leyens, C.; Walther, F. Defect-based characterization of the fatigue behavior of additively manufactured titanium aluminides. *Int. J. Fatigue* **2022**, *163*, 107047. [\[CrossRef\]](#)
55. Sanaei, N.; Fatemi, A. Defect-based fatigue life prediction of L-PBF additive manufactured metals. *Eng. Fract. Mech.* **2021**, *244*, 107541. [\[CrossRef\]](#)
56. Wu, Z.; He, Z.; Wu, S.; Gao, X.; Lei, L.; Liu, C.; Chen, B.; Dong, C. Rotating bending fatigue mechanisms of L-PBF manufactured Ti-6Al-4V alloys using in situ X-ray tomography. *Int. J. Fatigue* **2023**, *176*, 107876. [\[CrossRef\]](#)
57. Dragonfly. O. R. S. O. Inc. Montreal, Canada. 2021. Available online: [https://dev.theobjects.com/dragonfly\\_2021\\_1\\_release/contents.html](https://dev.theobjects.com/dragonfly_2021_1_release/contents.html) (accessed on 3 September 2024).
58. Murakami, Y. *Metal Fatigue: Effects of Small Defects and Nonmetallic Inclusions*; Elsevier: Amsterdam, The Netherlands, 2002.
59. Singh, S.N.; Deoghare, A.B. Microstructure, micro-hardness and tensile properties of Ti6Al4V manufactured by high layer-thickness wire-feed multi-laser directed energy deposition. *Mater. Lett.* **2023**, *340*, 134207. [\[CrossRef\]](#)
60. Sun, W.; Ma, Y.; Huang, W.; Zhang, W.; Qian, X. Effects of build direction on tensile and fatigue performance of selective laser melting Ti6Al4V titanium alloy. *Int. J. Fatigue* **2020**, *130*, 105260. [\[CrossRef\]](#)
61. Sun, W.; Ma, Y.E.; Zhang, W.; Qian, X.; Huang, W.; Wang, Z. Effects of the Build Direction on Mechanical Performance of Laser Powder Bed Fusion Additively Manufactured Ti6Al4V under Different Loadings. *Adv. Eng. Mater.* **2021**, *23*, 2100611. [\[CrossRef\]](#)

**Disclaimer/Publisher’s Note:** The statements, opinions and data contained in all publications are solely those of the individual author(s) and contributor(s) and not of MDPI and/or the editor(s). MDPI and/or the editor(s) disclaim responsibility for any injury to people or property resulting from any ideas, methods, instructions or products referred to in the content.